

Article

Sideslip Angle Estimation for Distributed Drive Electric Vehicles Based on Robust Unscented Particle Filter

Jie Hu^{1,2,3,4}, Feiyue Rong^{1,2,3}, Pei Zhang^{1,2,3,*}  and Fuwu Yan^{1,2,3}

- ¹ Hubei Key Laboratory of Advanced Technology for Automotive Components, Wuhan University of Technology, Wuhan 430070, China; auto_hujie@whut.edu.cn (J.H.); rongfy@whut.edu.cn (F.R.); yanfw@whut.edu.cn (F.Y.)
- ² Hubei Research Center for New Energy & Intelligent Connected Vehicle Engineering, Wuhan University of Technology, Wuhan 430070, China
- ³ Hubei Collaborative Innovation Center for Automotive Components Technology, Wuhan University of Technology, Wuhan 430070, China
- ⁴ Hubei Longzhong Laboratory, Wuhan University of Technology, Xiangyang 441000, China
- * Correspondence: zhangpei@whut.edu.cn

Abstract: An accurate and reliable sideslip angle is crucial for active safety control systems and advanced driver-assistance systems (ADAS). The direct measurement method of the sideslip angle suffers from challenges of high costs and environmental sensitivity, so sideslip angle estimation has always been a significant research issue. To improve the precision and robustness of sideslip angle estimation for distributed drive electric vehicles (DDEV) in extreme maneuvering scenarios, this paper presents a novel robust unscented particle filter (RUPF) algorithm based on low-cost onboard sensors. Firstly, a nonlinear dynamics model of DDEV is constructed, providing a theoretical foundation for the design of the RUPF algorithm. Then, the RUPF algorithm, which incorporates the unscented Kalman filter (UKF) to update importance density and utilizes systematic random resampling to mitigate particle degradation, is designed for estimation. Eventually, the availability of the proposed RUPF algorithm is validated on the co-simulation platform with non-Gaussian noises. Simulation results demonstrate that RUPF algorithm attains a higher precision and stronger robustness compared with the traditional PF and UKF algorithms.



Citation: Hu, J.; Rong, F.; Zhang, P.; Yan, F. Sideslip Angle Estimation for Distributed Drive Electric Vehicles Based on Robust Unscented Particle Filter. *Mathematics* **2024**, *12*, 1350. <https://doi.org/10.3390/math12091350>

Academic Editor: Pedro A. Castillo Valdivieso

Received: 20 March 2024

Revised: 12 April 2024

Accepted: 26 April 2024

Published: 29 April 2024



Copyright: © 2024 by the authors. Licensee MDPI, Basel, Switzerland. This article is an open access article distributed under the terms and conditions of the Creative Commons Attribution (CC BY) license (<https://creativecommons.org/licenses/by/4.0/>).

Keywords: distributed drive electric vehicles; sideslip angle; state estimation; robust unscented particle filter

MSC: 93-10

1. Introduction

With the advancement in intelligent connected electric vehicles, active safety control systems and advanced driver-assistance systems (ADASs) are progressively being implemented in mass-produced cars. Distributed drive electric vehicle (DDEV) relies on four in-wheel motors to achieve independent driving, braking, and steering. Due to its unique structure and the capability to quantify driving/braking forces, DDEV serves as an excellent platform for implementing active safety control systems and ADASs [1–3]. It is widely acknowledged that the devising of these active safety control systems and ADASs necessitates the real-time acquisition of vehicle-inherent information, for instance, yaw rate, sideslip angle, and vehicle longitudinal speed [4,5]. Among the aforementioned vehicle state information, the sideslip angle is a pivotal parameter in characterizing the vehicle's stability. The need for a precise sideslip angle is particularly pressing for vehicle motion control. Nevertheless, the direct measurement method of sideslip angles using Global Positioning System (GPS) and Inertial Navigation System (INS) or non-contact optical sensors suffers from challenges involving high costs and environmental sensitivity [6].

Consequently, current strategies predominantly rely on various algorithms for estimation. The cornerstone of vehicle state estimation involves employing low-cost sensors, leveraging vehicle dynamics principles, and integrating the unique attributes of DDEV to estimate the sideslip angle through information fusion.

Vehicle sideslip angle estimation methodologies are principally categorized into three primary groups, direct integration methods based on kinematics, state observer methods based on dynamics, and data-driven methods based on neural networks (NN) [7–9], as illustrated in Figure 1.

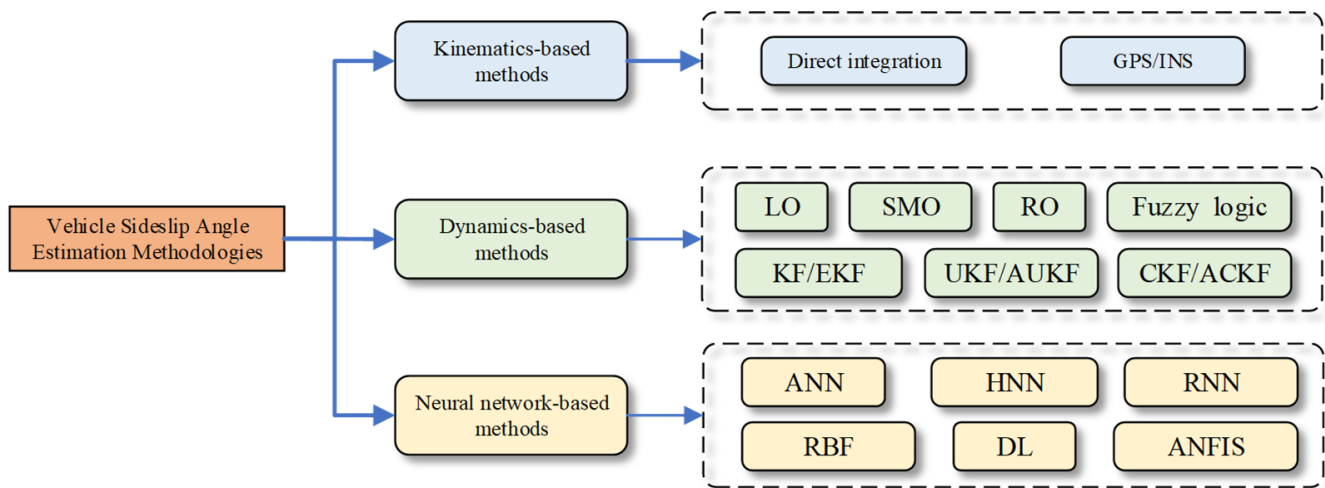


Figure 1. Commonly used methods for estimating sideslip angle.

Sideslip angle estimation based on kinematics primarily involves directly integrating the sensor signals or constructing an estimator via GPS/INS. Li et al. [10] compared the direct integration method with other estimation techniques in practical experiments. Bevely et al. [11] built a classic bicycle model and combined INS with GPS measurements to obtain superior accuracy of the sideslip angle. The methods based on kinematics demonstrate notable robustness but are heavily dependent on sensor accuracy. The sensor errors tend to accumulate during integration, particularly for lateral acceleration, which is susceptible to various internal and external factors [12]. Moreover, model-free neural networks provide alternative methods for sideslip angle estimation, encompassing artificial neural network (ANN), hybrid neural network (HNN), recurrent neural network (RNN), radial basis function (RBF), adaptive neuro-fuzzy inference system (ANFIS), and other deep learning (DL)-based approaches. Chindamo et al. [13] employed a 5-10-1 ANN architecture to forecast the vehicle sideslip angle, aimed at enhancing the efficacy of automotive active safety systems. Gao et al. [14] designed an estimation algorithm based on HNN, leveraging vehicle dynamics characteristics to achieve precise state estimation without relying on a dynamic model. Gräber et al. [15] demonstrated how to integrate RNN with kinematic models, thus proposing a supervised machine learning scheme for sideslip angle estimation. Zha et al. [16] combined the model-driven algorithm with the data-driven RBF neural network approach and employed the dichotomy method to implement weighted fusion of the estimation results, thereby enhancing the accuracy of estimation. Based on cheap sensors, Boada et al. [17] utilized the ANFIS for sideslip angle estimation. Furthermore, Ghosh et al. [18] drew an observer based on DL networks for robustly estimating sideslip angles in all-wheel-drive vehicles. Neural-network-based methods typically yield more accurate estimation results. However, this kind of estimation method requires substantial volumes of data for parameter training and consumes more computational resources during algorithm execution.

Dynamics-based estimation methods for sideslip angle can significantly mitigate reliance on sensor accuracy and are currently the predominant methods in the field, involving

methods such as Luenberger observer (LO), sliding mode observer (SMO), robust observer (RO), fuzzy logic control, and Kalman filter (KF) and its various variations. Ding et al. [19] utilized the LO for estimation based on a simplified bicycle model. Chen et al. [20] developed an SMO by utilizing the accurate UniTire model, which not only lessened the computational load but also yielded favorable estimation outcomes. Chen et al. [21] developed an RO with regional stability constraints, and higher estimation accuracy was achieved compared to the LO. Cheli et al. [22] employed fuzzy logic control to enhance the estimation accuracy of integrated observers based on kinematics and dynamics.

Among dynamics-based approaches, Kalman filter-based estimation methods have exhibited good robustness for model inaccuracies and environmental noise and real-time computation, and have been considered as the leading estimation technique in contemporary applications. Anderson et al. [23] integrated GPS and INS measurements via a KF for estimation. Given that vehicle systems exhibit strong nonlinear behavior, while traditional Kalman filters are designed for linear systems, several variants of Kalman filter have emerged, including extended Kalman filter (EKF), unscented Kalman filter (UKF), and cubature Kalman filter (CKF), etc. The EKF approach linearizes the nonlinear system and preserves the first-order Taylor expansion term, facilitating the handling of nonlinearity. Reina et al. [24] addressed the impact of tire-cornering stiffness on sideslip angle estimation by proposing an augmented EKF to accommodate model parameter variability. Nonetheless, the EKF methodology needs to solve the Jacobian matrix and ensure the continuous accumulation of linearization errors. The UKF employs unscented transformation (UT) to approximate the probability density distribution (PDF) of functions, and utilizes a determined set of sample Sigma points to approach posterior probability density. The second-order Taylor expansion term would be maintained in the linearization of UKF. Wang et al. [25] developed a UKF algorithm, and also conducted joint simulation tests to verify the enhanced accuracy of the UKF algorithm across various operational conditions. Strano et al. [26] implemented a constrained UKF to lighten the impact of measurement noise and nonlinearity on sideslip angle estimation. The CKF employs special rules to select volume points, offering a systematic approach to solving high-dimensional challenges [27]. On the basis of a nonlinear three-degrees-of-freedom (3-DOF) vehicle model, Xin et al. [28] introduced a CKF algorithm for estimating sideslip angle by merely utilizing common onboard sensors. Furthermore, algorithms such as the fuzzy adaptive robust CKF and the weighted square root CKF have also been applied for estimation [29,30].

However, the KF and its various derivatives are optimally suited for scenarios where both process and measurement noises adhere to Gaussian distributions. In fact, the statistical properties of the noises during actual driving conditions remain uncertain, so the estimation accuracy of Kalman filter-based methods would significantly diminish in a real-time estimation of sideslip angle, especially for vehicular nonlinearity without assuming that noises follow Gaussian distributions.

As a statistical approach founded on sequential Monte Carlo (SMC) methods, the particle filter (PF) effectively implements the recursive Bayesian filter (RBF) for estimation in nonlinear, non-Gaussian systems. Therefore, PF has been reckoned as a solution to address the constraints of vehicle nonlinear systems and non-Gaussian noise that Kalman filter-based methods have suffered [31]. However, PF faces challenges from importance density identification and particle degradation [32]. As the number of iterations increases, most particles with minimal weights become scarce or vanish, and thus particle diversity diminishes significantly. Particle degradation not only leads to the squandering of substantial computational resources on inconsequential particle computations but also impairs the accuracy of the outcomes. To mitigate particle degradation, commonly employed strategies include increasing the amount of particles, implementing resampling techniques, and designing a reasonable importance density [33–35]. The core idea behind increasing the number of particles is to enhance particle diversity and decelerate particle degradation. Nevertheless, the increase in particle quantity will result in a higher computational time, rendering it unsuitable for real-time vehicular control systems. Resampling techniques

involve polynomial resampling, systematic random resampling, etc. Systematic random resampling, noted for its low computational complexity, can enhance the efficacy of the PF algorithm. Ultimately, choosing an appropriate importance density ensures the validity of the particles. The traditional PF algorithm selects the posterior PDF of the state transition as the importance density, making the updates of particle weight at any given moment only relate to the previous state. Hence, the traditional PF algorithm cannot fully utilize the latest measurement information, ultimately reducing the estimation accuracy.

To address the identified research deficiencies and increase the precision and robustness of sideslip angle estimation, this study presented a robust unscented particle filter (RUPF) algorithm by combining PF and UKF. Given the uncertainties associated with process and measurement noise, the RUPF algorithm adopts the PF algorithm as its core framework. To overcome the challenge of selecting an appropriate importance density, the UKF is utilized to update the importance density with real-time observational information. Additionally, systematic random resampling is implemented to reduce particle degradation, thereby enhancing the algorithm's accuracy and robustness in estimating the sideslip angle.

The main contributions are summarized as follows:

- (1) A RUPF algorithm, leveraging low-cost onboard sensors, is devised to estimate the sideslip angle. The importance density is initially updated in real time using the UKF, followed by the application of systematic stochastic resampling to counteract particle degradation.
- (2) Three performance metrics are introduced to quantitatively assess the precision of the RUPF algorithm, and the precision and robustness of RUPF are thoroughly validated through simulation tests under different maneuver scenarios.

The rest of this paper is organized as follows: Section 2 gives a detailed construction method for a DDEV dynamics model. Section 3 illustrates the design process of the RUPF algorithm. Simulation comparative analysis is provided to demonstrate the advantage of the proposed approach with different scenario tests in Section 4. Finally, conclusions and outlooks are discussed in Section 5.

2. Vehicle Dynamics Model

The vehicle dynamics model is the foundation for vehicle sideslip angle estimation. The RUPF estimation algorithm necessitates the consideration of the observer's real-time capabilities and the model's precision. Typically, the DDEV dynamics model comprises two primary components, a vehicle body model and a tire model, which are delineated separately in the subsequent sections. Based on the DDEV dynamics model, state-of-system equations and measurement equations necessary for the RUPF algorithm in discrete time are also illustrated.

2.1. Nonlinear 3-DOF Dynamics Model

Balancing model simplification with real-time algorithm requirements, this paper develops a nonlinear 3-DOF model that encompasses longitudinal, lateral, and yaw movements. As displayed in Figure 2, the dynamics model restricts vehicle movement to the xoy plane, and the vehicle's center of gravity (CoG) aligns with the coordinate system's origin. Here, x represents the longitudinal motion, while y corresponds to its lateral direction. Additionally, the model incorporates the following assumptions [36]: (1) disregarding the effect of the steering system, input parameter is defined as front wheel steering angle; (2) the effects of suspension system are neglected, along with vertical wheel runout; (3) the dynamics of each tire are considered identical; and (4) the influences of air resistance and rolling resistance are overlooked.

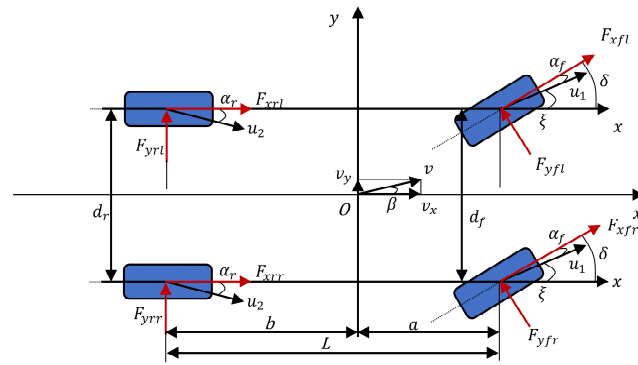


Figure 2. Nonlinear 3-DOF dynamics model.

The equilibrium equations for the nonlinear 3-DOF vehicle dynamics model are delineated below:

$$m(\dot{v}_x - v_y\gamma) = (F_{xfl} + F_{xfr})\cos\delta - (F_{yfl} + F_{yfr})\sin\delta + F_{xrl} + F_{xrr} \quad (1)$$

$$m(\dot{v}_y + v_x\gamma) = (F_{xfl} + F_{xfr})\sin\delta + (F_{yfl} + F_{yfr})\cos\delta + F_{yrl} + F_{yrr} \quad (2)$$

$$I_z\dot{\gamma} = [(F_{xfr} - F_{xfl})\cos\delta + (F_{yfl} - F_{yfr})\sin\delta]\frac{d_f}{2} + (F_{xrr} - F_{xrl})\frac{d_r}{2} + [(F_{xfl} + F_{xfr})\sin\delta + (F_{yfl} + F_{yfr})\cos\delta]a - (F_{yrl} + F_{yrr})b \quad (3)$$

where m is vehicle mass; L is wheelbase, $L = a + b$; a and b are distance from CoG to axles; d_f and d_r are track width of axles, respectively; I_z is yaw inertia moment; δ is on behalf of front wheel steering angle; α_f and α_r are slip angle of front and rear wheels; v_x and v_y are longitudinal and lateral speeds; γ is yaw rate; β is sideslip angle; F_{xij} is longitudinal force exerted on wheels; F_{yij} is lateral force; and $ij = fl, fr, rl, rr$, which stands for left front, right front, left rear, and right rear wheels, respectively.

The sideslip angle is deduced from the inverse tangent of the rate of lateral to longitudinal vehicle speeds, and its numerical value is generally small (ranging from -5° to 5°). For the sake of simplifying calculations, it can be approximated as follows:

$$\beta = \arctan\left(\frac{v_y}{v_x}\right) \approx \frac{v_y}{v_x} \quad (4)$$

The linear tire model is more effective in characterizing tire forces in the case of lateral acceleration within 0.4 g. Consequently, lateral forces can be represented as follows:

$$\begin{cases} F_{yf} = k_f\alpha_f \\ F_{yr} = k_r\alpha_r \end{cases} \quad (5)$$

where k_f and k_r represent the cornering stiffnesses of axles; F_{yf} is the lateral force on the front axle, $F_{yf} = F_{yfl} + F_{yfr}$; and F_{yr} is the lateral force on the rear axle, $F_{yr} = F_{yrl} + F_{yrr}$.

In the presence of a small tire slip angle, there exists a small-angle approximation. The slip angle of wheels can be described as below:

$$\begin{cases} \alpha_f = (v_y + a\gamma)/v_x - \delta \\ \alpha_r = (v_y - b\gamma)/v_x \end{cases} \quad (6)$$

Through Equations (1)–(6), state space equations of DDEV can be simplified as below:

$$\begin{cases} \dot{\gamma} = \frac{a^2k_f + b^2k_r}{I_z v_x} \gamma + \frac{ak_f - bk_r}{I_z} \beta - \frac{ak_f}{I_z} \delta \\ \dot{\beta} = \left(\frac{ak_f - bk_r}{m v_x^2} - 1\right) \gamma + \frac{k_f + k_r}{m v_x} \beta - \frac{k_f}{m v_x} \delta \\ \dot{v}_x = \gamma\beta v_x + a_x \end{cases} \quad (7)$$

2.2. Tire Model

As the exclusive interface between the vehicle and the ground, tires predominantly convey the system’s nonlinear properties. The Dugoff model, derived from the Magic Formula model, effectively encapsulates nonlinear characteristics of vehicle tires. The Dugoff tire model offers a more streamlined parameter fitting process than the Magic Formula tire model and boasts computational simplicity compared to the UniTire model. Thus, this study chose the Dugoff model to simulate the tire, which is articulated as follows [37]:

$$\begin{cases} F_x = C_x \frac{\lambda}{1-\lambda} f(L) \\ F_y = C_y \frac{\tan \alpha}{1-\lambda} f(L) \end{cases} \tag{8}$$

$$f(L) = \begin{cases} 1 & , L \geq 1 \\ L(2-L) & , L < 1 \end{cases} \tag{9}$$

$$L = \frac{\mu F_z (1-\lambda)}{2\sqrt{C_x^2 \lambda^2 + C_y^2 \tan^2 \alpha}} \left(1 - \varepsilon v \sqrt{C_x^2 \lambda^2 + C_y^2 \tan^2 \alpha} \right) \tag{10}$$

where C_x and C_y are the longitudinal and lateral cornering stiffnesses of tires; μ is the road adhesion coefficient; and ε is the velocity impact factor.

To enhance the precision of the Dugoff model, the cornering stiffnesses are calculated by the following equation:

$$\begin{cases} C_x = a_0 B_x (a_1 F_z^2 + a_2 F_z) \\ C_y = b_0 B_y (b_1 F_z^2 + b_2 F_z) \end{cases} \tag{11}$$

where $a_0, a_1, a_2, b_0, b_1,$ and b_2 are the fitting coefficients, and B_x and B_y are tire stiffness factors, as represented in Table 1.

Table 1. The fitting coefficients of the Dugoff model.

Coefficient	a_0	a_1	a_2	b_0	b_1	b_2	B_x	B_y
Value	1.42	−11.03	1037	1.38	−5.67	976	0.6766	0.1559

Throughout the vehicle’s operation, the vertical load on each wheel varies due to steering and braking, which can be computed as follows:

$$\begin{cases} F_{zfl} = mg \frac{b}{2L} - ma_x \frac{h_g}{2L} - ma_y \frac{bh_g}{Ld_f} \\ F_{zfr} = mg \frac{b}{2L} - ma_x \frac{h_g}{2L} + ma_y \frac{bh_g}{Ld_f} \\ F_{zrl} = mg \frac{a}{2L} + ma_x \frac{h_g}{2L} - ma_y \frac{bh_g}{Ld_f} \\ F_{zrr} = mg \frac{a}{2L} + ma_x \frac{h_g}{2L} + ma_y \frac{bh_g}{Ld_f} \end{cases} \tag{12}$$

The slip angle of each tire is:

$$\begin{cases} \alpha_{fl} = \delta - \arctan\left(\frac{(v_y + a\gamma)}{(v_x - 0.5d_f\gamma)}\right) \\ \alpha_{fr} = \delta - \arctan\left(\frac{(v_y + a\gamma)}{(v_x + 0.5d_f\gamma)}\right) \\ \alpha_{rl} = -\arctan\left(\frac{(v_y - b\gamma)}{(v_x - 0.5d_r\gamma)}\right) \\ \alpha_{rr} = -\arctan\left(\frac{(v_y - b\gamma)}{(v_x + 0.5d_r\gamma)}\right) \end{cases} \tag{13}$$

The longitudinal velocity of each tire is denoted, respectively, as:

$$\begin{cases} v_{fl} = (v_x - 0.5d\gamma) \cos \delta + (v_y + a\gamma) \sin \delta \\ v_{fr} = (v_x + 0.5d\gamma) \cos \delta + (v_y + a\gamma) \sin \delta \\ v_{rl} = v_x - 0.5d\gamma \\ v_{rr} = v_x + 0.5d\gamma \end{cases} \tag{14}$$

The longitudinal tire slip ratios of wheels are denoted, respectively, as:

$$\lambda_{ij} = \frac{\omega_{ij}R - v_{ij}}{\max(\omega_{ij}R, v_{ij})} \tag{15}$$

where F_{zij} is vertical tire load; α_{ij} is tire slip angle; λ_{ij} is slip ratio; ω_{ij} is rotational angular velocity of wheels; h_g is height of vehicle's CoG; R is effective tire radius; g is the acceleration of gravity; and d is an average value of track width, $d = (d_f + d_r)/2$.

The wheel rotational dynamics model is illustrated in Figure 3. The equation for each wheel can be denoted as [38]:

$$J\dot{\omega}_{ij} = T_{dij} - F_{xij}R \tag{16}$$

where J is wheel moment of inertia and T_{dij} is motor driving torque.

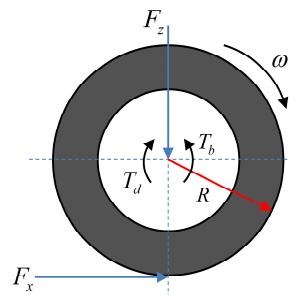


Figure 3. Wheel rotational dynamics model.

2.3. Discretization of System and Measurement Equations

Both system and measurement equations for sideslip angle estimation should be discretized to implement the subsequent RUPF estimation algorithm.

As outlined in Equation (7), the time-continuous state x can be defined as follows:

$$x = [\gamma \quad \beta \quad v_x]^T \tag{17}$$

The continuous-time control input u is defined as:

$$u = [\delta \quad a_x]^T \tag{18}$$

Through Equations (2), (4)–(6), the measurement equation is simplified as:

$$z = [a_y] = \frac{ak_f - bk_r}{mv_x} \gamma + \frac{k_f + k_r}{m} \beta - \frac{k_f}{m} \delta \tag{19}$$

where a_x and a_y are the longitudinal and lateral acceleration.

From Equations (7), (17)–(19), the time-continuous system and measurement formulas can be derived:

$$\begin{cases} \dot{x}(t) = f(x(t), u(t)) + w(t) \\ z(t) = h(x(t), u(t)) + v(t) \end{cases} \tag{20}$$

Equation (20) can be further discretized as:

$$\begin{cases} x_{k+1} = f(x_k, u_k) + w_k \\ z_k = h(x_k, u_k) + v_k \end{cases} \tag{21}$$

where x_k is discrete system state variable; z_k is discrete system measurement variable; u_k is the system input control; w_k and v_k are process and measurement noises; and $k, k + 1$ represent sampling moments.

3. The Design of the RUPF Algorithm for Sideslip Angle Estimation

In this section, the RUPF algorithm incorporating PF and UKF algorithms for sideslip angle estimation is discussed. The flowchart of the RUPF algorithm is displayed in Figure 4.

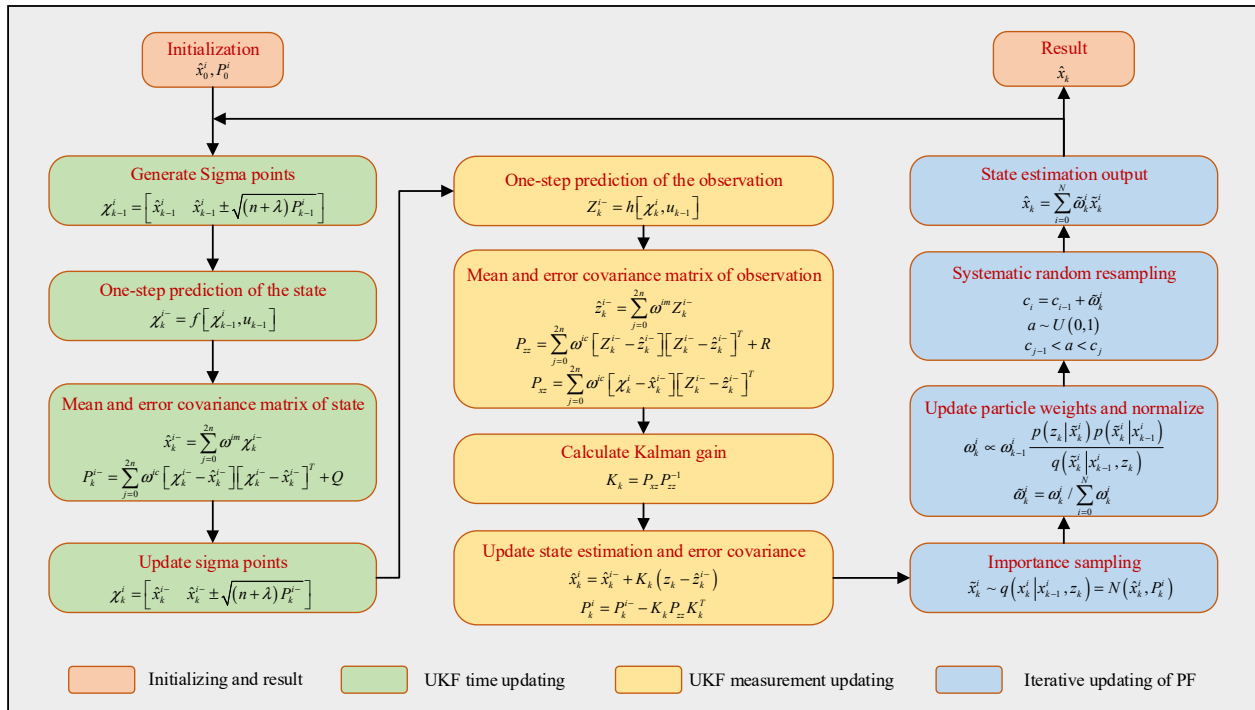


Figure 4. The flowchart of the RUPF algorithm.

For the nonlinear discrete system described in Equation (21), the procedure for the RUPF algorithm involves the following steps:

(1) Initialization ($k = 0$): sample N particles $\{x_0^i\}_{i=1}^N$ with same weights $1/N$ generated by the prior PDF $p(x_0)$:

$$\hat{x}_0^i = E[x_0^i], P_0^i = E[(x_0^i - \hat{x}_0^i)(x_0^i - \hat{x}_0^i)^T] \tag{22}$$

(2) Calculate the importance density using UKF when $k = 1, 2, \dots$:
Construct Sigma points based on symmetric sampling strategy:

$$\begin{cases} \chi_{(0)}^i = \hat{x}_0^i & , l = 0 \\ \chi_{(l)}^i = \hat{x}_0^i + \left(\sqrt{(n+\lambda)P_0^i} \right)_l & , l = 1, 2, \dots, n \\ \chi_{(l)}^i = \hat{x}_0^i - \left(\sqrt{(n+\lambda)P_0^i} \right)_l & , l = n+1, \dots, 2n \end{cases} \tag{23}$$

Calculate the Sigma points' weight:

$$\begin{cases} \omega_{(0)}^{im} = \frac{\lambda}{n+\lambda} & , l = 0 \\ \omega_{(0)}^{ic} = \frac{\lambda}{n+\lambda} + (1 - \alpha^2 + \beta) & , l = 0 \\ \omega_{(l)}^{im} = \omega_{(l)}^{ic} = \frac{1}{2(n+\lambda)} & , l = 1, 2, \dots, 2n \\ \lambda = \alpha^2(n + \kappa) - n \end{cases} \tag{24}$$

where \hat{x}_0^i and P_0^i are the averages of the system states and error covariance matrix; m is the weight of the states and c is the weight of P_0^i ; λ is scaling function; α is utilized to control

distribution function ($10^{-4} \leq \alpha \leq 1$); κ is the second-order scaling parameter, $\kappa = 0$ when $n > 3$, $\kappa = 3 - n$ when $n \leq 3$; and β is the weighting factor, which is defined as 2 according to a large number of experiences.

The UT is utilized to generate the Sigma points set:

$$\chi_{k-1}^i = \left[\hat{x}_{k-1}^i \hat{x}_{k-1}^i + \sqrt{(n + \lambda)P_{k-1}^i} \hat{x}_{k-1}^i - \sqrt{(n + \lambda)P_{k-1}^i} \right] \tag{25}$$

One-step prediction of the points is computed as follows:

$$\chi_k^{i-} = f \left[\chi_{k-1}^i, u_{k-1} \right] \tag{26}$$

Calculate the state mean and error covariance matrix:

$$\hat{x}_k^{i-} = \sum_{j=0}^{2n} \omega^{im} \chi_k^{i-} \tag{27}$$

$$P_k^{i-} = \sum_{j=0}^{2n} \omega^{ic} \left[\chi_k^{i-} - \hat{x}_k^{i-} \right] \left[\chi_k^{i-} - \hat{x}_k^{i-} \right]^T + Q \tag{28}$$

Based on the one-step prediction, a new series of points is generated by the UT:

$$\chi_k^i = \left[\hat{x}_k^{i-} \hat{x}_k^{i-} + \sqrt{(n + \lambda)P_k^{i-}} \hat{x}_k^{i-} - \sqrt{(n + \lambda)P_k^{i-}} \right] \tag{29}$$

Calculate the observed predicted values for the Sigma points:

$$Z_k^{i-} = h \left[\chi_k^i, u_{k-1} \right] \tag{30}$$

The observed predictions are weighted to find the mean and error covariance matrix of the systematic observed predictions:

$$\hat{z}_k^{i-} = \sum_{j=0}^{2n} \omega^{im} Z_k^{i-} \tag{31}$$

$$P_{zz} = \sum_{j=0}^{2n} \omega^{ic} \left[Z_k^{i-} - \hat{z}_k^{i-} \right] \left[Z_k^{i-} - \hat{z}_k^{i-} \right]^T + R \tag{32}$$

Calculate the inter-correlation error covariance matrix:

$$P_{xz} = \sum_{j=0}^{2n} \omega^{ic} \left[\chi_k^i - \hat{x}_k^{i-} \right] \left[Z_k^{i-} - \hat{z}_k^{i-} \right]^T \tag{33}$$

Calculate the Kalman gain matrix:

$$K_k = P_{xz} P_{zz}^{-1} \tag{34}$$

Update state estimation and error covariance matrix:

$$\hat{x}_k^i = \hat{x}_k^{i-} + K_k \left(z_k - \hat{z}_k^{i-} \right) \tag{35}$$

$$P_k^i = P_k^{i-} - K_k P_{zz} K_k^T \tag{36}$$

(3) Importance sampling, sampling particles:

$$\tilde{x}_k^i \sim q \left(x_k^i \mid x_{k-1}^i, z_k \right) = N \left(\hat{x}_k^i, P_k^i \right) \tag{37}$$

where $N(\cdot)$ is a Gaussian function.

(4) Update particle weights and normalize:

$$\omega_k^i \propto \omega_{k-1}^i \frac{p(z_k | \tilde{x}_k^i) p(\tilde{x}_k^i | x_{k-1}^i)}{q(\tilde{x}_k^i | x_{k-1}^i, z_k)} \tag{38}$$

$$\tilde{\omega}_k^i = \omega_k^i / \sum_{i=0}^N \omega_k^i \tag{39}$$

(5) Systematic random resampling:

① Initialization of the cumulative distribution function (CDF): $c_0 = 0$;

② Assign the CDF;

$$c_i = c_{i-1} + \tilde{\omega}_k^i \tag{40}$$

③ For N particles, generate random numbers separately:

$$a \sim U(0, 1) \tag{41}$$

Find the integer j that satisfies the following equation, where $j = 1, 2, \dots, N$:

$$c_{j-1} < a < c_j \tag{42}$$

Copy the j th particle once and assign it to the new particle; the particle weights are reset to $1/N$, and a total of N new particles are generated after the resampling;

(6) State the estimation output at the moment k .

$$\hat{x}_k = \sum_{i=0}^N \tilde{\omega}_k^i \tilde{x}_k^i \tag{43}$$

The pseudocode of the RUPF algorithm is displayed in Algorithm 1.

Algorithm 1: Robust Unscented Particle Filter Algorithm

- 1: Initialize filter parameters: particle number N ; total simulation time t ; time step T ;
 - 2: Initialize the vehicle parameters to be estimated: \hat{x}_0^i, P_0^i ;
 - 3: **for** $k = T:T:t$ **do**
 - 4: **for** $i = 1:N$ **do**
 - 5: generate Sigma points set: χ_{k-1}^i ;
 - 6: calculate the priori state estimate: χ_k^{i-} ;
 - 7: generate a new set of Sigma points: χ_k^i ;
 - 8: calculate the priori measurement: Z_k^{i-} ;
 - 9: calculate the UKF gain: K_k ;
 - 10: update the variables of state and error covariance matrix: \hat{x}_k^i, P_k^i ;
 - 11: **end for**
 - 12: importance resampling: \tilde{x}_k^i ;
 - 13: update particle weights and normalize: $\tilde{\omega}_k^i$;
 - 14: initialize the CDF: c_0 ;
 - 15: assign cumulative weights to CDF;
 - 16: **for** $j = 1:N$ **do**
 - 17: systematic random resampling;
 - 18: **end for**
 - 19: state estimation results: \hat{x}_k ;
 - 20: **end for**
-

4. Simulation Results and Discussion

In order to demonstrate the feasibility and effectiveness of the RUPF algorithm, a co-simulation platform is built as illustrated in Figure 5, which consists of four main sub-

modules: the distributed drive electric vehicle system, data acquisition system, sideslip angle estimation system, and evaluation system. Due to the current absence of the DDEV model within the Carsim software, a virtual model of DDEV based on the Carsim/Simulink software is constructed in the first submodule. The communication connection between Carsim and Simulink is realized through the Carsim-S function. Moreover, classical experiments, including double lane change (DLC) and slalom tests, designed to assess the stability of automobile maneuvering under high- and low-adhesion roads, are executed on the virtual DDEV. The data acquisition system simulates real unknown noise environments. Subsequently, the proposed RUPF algorithm and traditional PF and UKF algorithms are designed for estimation. Estimation results of RUPF, PF, and UKF are quantitatively evaluated and compared across three performance metrics in the fourth submodule.

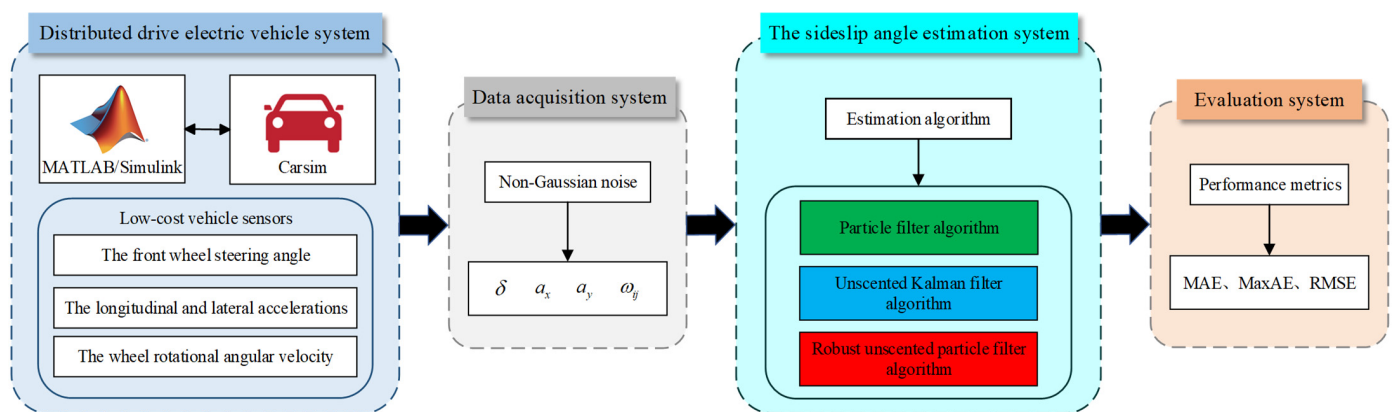


Figure 5. The co-simulation platform for vehicle sideslip angle estimation.

4.1. Simulation Setup

The particular testing criteria are guided by ISO 15037-1:2019 and ISO 3888-1:2018 standards [39,40]. In this study, μ is set to 0.85 for dry and uniform paved road surfaces, while for icy or snowy road surfaces, it is set to 0.35. For the DLC tests, the vehicle speeds are set at 80 km/h and 30 km/h, while for slalom tests, they are set at 60 km/h and 35 km/h, respectively. Considering practical constraints, this study refrained from conducting high-speed DLC and slalom tests on road surfaces with low adhesion.

The major parameters of the DDEV are sourced from the full-size SUV in Carsim software, as depicted in Table 2.

Table 2. The major parameters of DDEV.

Parameters	Symbol	Unit	Value
Vehicle mass	m	kg	2532
Distance from vehicle CoG to front axle	a	m	1.33
Distance from vehicle CoG to rear axle	b	m	1.81
Height of vehicle CoG	h_g	m	0.781
Front track width	d_f	m	1.725
Rear track width	d_r	m	1.750
Yaw moment of inertia	I_z	kg·m ²	3524.9
Effective tire radius	R	m	0.368
Wheel moment of inertia	J	kg·m ²	1.1
Rated power of the motor	P	kW	30

To further illustrate the superiority of the RUPF algorithm, three performance metrics—mean absolute error (MAE), maximum absolute error (MaxAE), and root mean square error (RMSE)—are employed for a quantitative comparison of estimation outcomes. MAE indicates the average magnitude of the estimation errors, MaxAE assesses the maximum

deviation between the estimated and reference values, and *RMSE* evaluates the tracking accuracy and robustness of the estimation results. Three performance metrics are calculated using the following formulas:

$$MAE = \frac{1}{N} \sum_{i=1}^N |y_i - \hat{y}_i| \tag{44}$$

$$MaxAE = \max \left[\frac{1}{N} \sum_{i=1}^N |y_i - \hat{y}_i| \right] \tag{45}$$

$$RMSE = \sqrt{\frac{1}{N} \sum_{i=1}^N (y_i - \hat{y}_i)^2} \tag{46}$$

where \hat{y}_i is the estimation results of algorithms, y_i represents the reference value from the Carsim, and N represents the number of simulation runs.

4.2. DLC Tests

The DLC test simulates the vehicle’s lane-keeping capability during emergency closed-loop control in actual driving, involving overtaking and emergency avoidance. It is a significant test condition for evaluating vehicle handling stability. Inputs for the high-vehicle-speed DLC test are depicted in Figure 6, while the corresponding simulation outcomes are depicted in Figure 7.

Figure 7 demonstrates that the UKF, PF, and RUPF algorithms can precisely estimate the vehicle sideslip angle with an error margin not exceeding 0.21° . The above prediction accuracy satisfies the demands of active safety control and ADAS. Additionally, it can be observed that the RUPF algorithm exhibits a smaller error margin in sideslip angle estimation. In Figure 7b, there is almost no error in the estimation of the RUPF algorithm during 0–2 s and 8–12 s, demonstrating a significant improvement over PF and UKF algorithms. A comparative analysis of three evaluation metrics on the high adhesion road is presented in Table 3. Regarding the *MAE* performance metric, the estimation results obtained by the RUPF algorithm demonstrate an improvement in accuracy of 16.3% and 16.9% compared to UKF and PF algorithms, respectively. Meanwhile, as for *MaxAE*, the RUPF algorithm shows enhancements of 16.5% and 17.7%, respectively. Compared with traditional algorithms, the *RMSE* has improved by 13.2% and 13.6%.

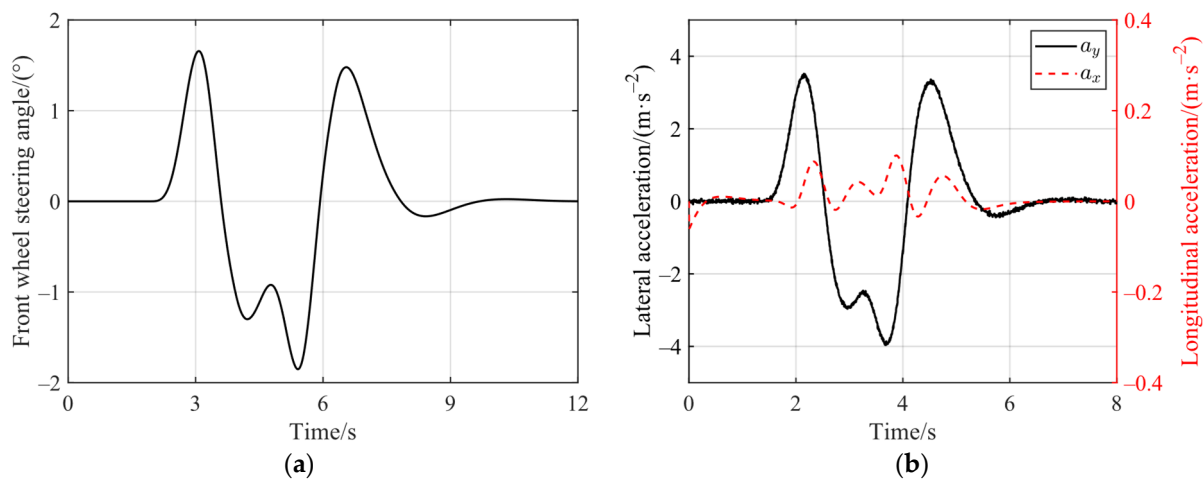


Figure 6. The inputs of high-vehicle-speed DLC test ($\mu = 0.85$). (a) The front wheel steering angle; (b) longitudinal and lateral acceleration (with non-Gaussian noise).

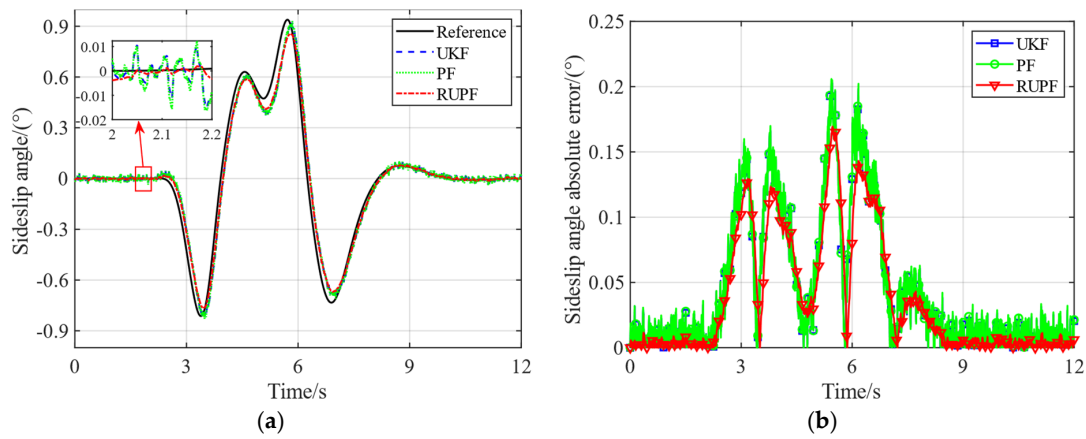


Figure 7. Simulation results of the high-vehicle-speed DLC test ($\mu = 0.85$). (a) Sideslip angle; (b) sideslip angle absolute error.

Table 3. MAE, MaxAE, and RMSE of the algorithms under high-vehicle-speed DLC test with high road adhesion coefficient.

80 km/h	MAE	MaxAE	RMSE
UKF	0.0447	0.2028	0.0682
PF	0.0450	0.2059	0.0685
RUPF	0.0374	0.1694	0.0592

Inputs for the low-vehicle-speed DLC test are illustrated in Figure 8, and the associated simulation outcomes are showcased in Figure 9.

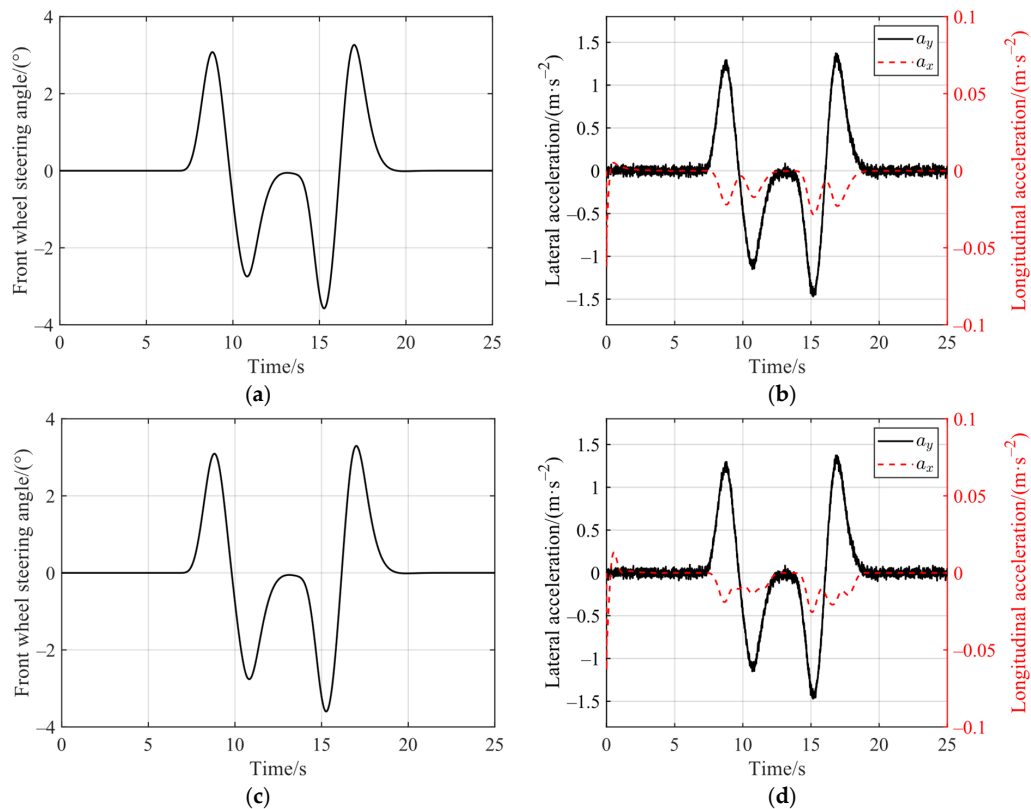


Figure 8. The inputs of low-vehicle-speed DLC tests. (a) The front wheel steering angle ($\mu = 0.85$); (b) longitudinal and lateral acceleration ($\mu = 0.85$); (c) the front wheel steering angle ($\mu = 0.35$); (d) longitudinal and lateral acceleration ($\mu = 0.35$).

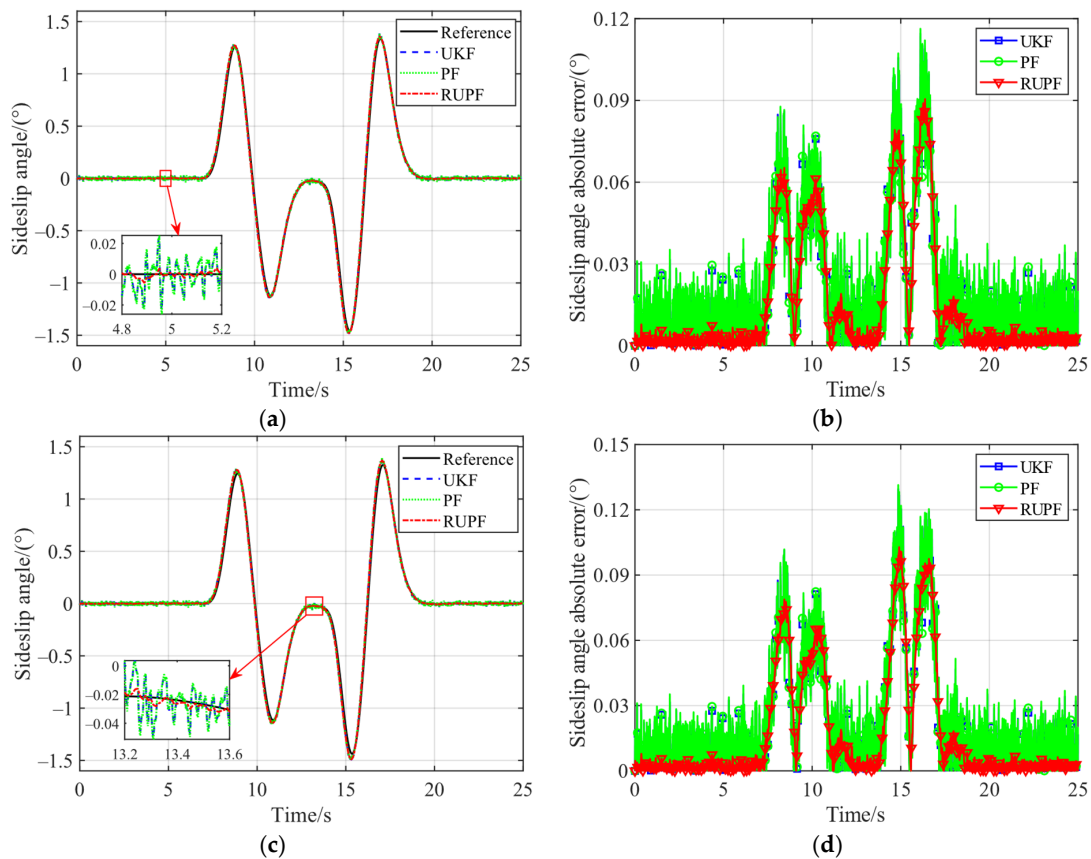


Figure 9. Simulation results of low-vehicle-speed DLC tests. (a) Sideslip angle ($\mu = 0.85$); (b) sideslip angle absolute error ($\mu = 0.85$); (c) sideslip angle ($\mu = 0.35$); (d) sideslip angle absolute error ($\mu = 0.35$).

The simulation results for the low-vehicle-speed DLC test are depicted in Figure 9. Despite the reduced speed, the three algorithms employed for sideslip angle estimation closely approximated the reference value, with an algorithmic error not exceeding 0.13° and a relative error below 10%. In Figure 9b,d, the absolute error in sideslip angle estimation generated by the RUPF algorithm is significantly smaller compared to the UKF and PF algorithms. At the same time, the errors generated during the DLC test on high-road-adhesion coefficient surfaces are smaller compared to those on low-adhesion surfaces. This is because the DDEV exhibits stronger nonlinear characteristics on low-road-adhesion coefficient surfaces. As indicated in Table 4, on dry and uniform paved roads, the accuracy and robustness of the RUPF algorithm show improvements of 24.6%, 21.0%, and 10.4% for three evaluation metrics when compared to the UKF algorithm, and enhancements of 26.1%, 22.2%, and 10.7% in comparison to the PF algorithm. When on icy or snowy road surfaces, the improvement is 21.9%, 20.6%, 8.7% and 23.3%, 21.8%, 9.0%, respectively. In relative terms, the estimation efficacy is superior under high-adhesion roads.

Table 4. MAE, MaxAE, and RMSE of the algorithms under low-vehicle-speed DLC tests.

30 km/h	$\mu = 0.85$			$\mu = 0.35$		
	MAE	MaxAE	RMSE	MAE	MaxAE	RMSE
UKF	0.0195	0.1146	0.0298	0.0219	0.1295	0.0344
PF	0.0199	0.1163	0.0299	0.0223	0.1314	0.0345
RUPF	0.0147	0.0905	0.0267	0.0171	0.1028	0.0314

4.3. Slalom Tests

To further underscore the superiority of the RUPF algorithm, slalom simulation tests are also conducted, representing typical extreme maneuvering scenarios. Inputs of the high vehicle speed slalom test are displayed in Figure 10.

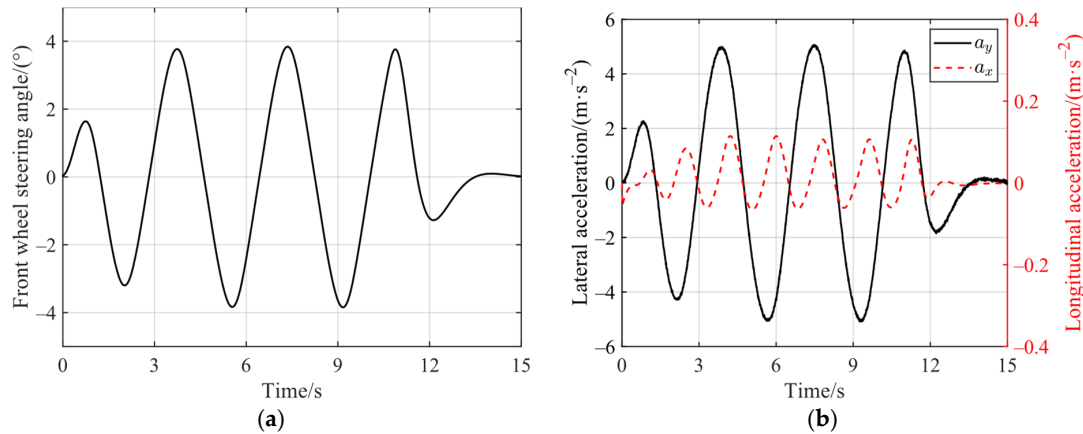


Figure 10. The inputs of the high-vehicle-speed slalom test ($\mu = 0.85$). (a) The front wheel steering angle; (b) longitudinal acceleration and lateral acceleration (with non-Gaussian noise).

The results with high speed are revealed in Figure 11. The vehicle’s peak lateral acceleration exceeded $4 \text{ m} \cdot \text{s}^{-2}$, indicating that the vehicle had entered a distinct phase of nonlinear control. As seen in Figure 11a, the estimated values from all three estimation algorithms can track the trend of the actual values. Due to the inherent nonlinear characteristics of the vehicle, the estimation results exhibit a slight deviation from the reference value. Nevertheless, it is evident that the errors obtained by the RUPF algorithm are the smallest. More details of the three performance metrics are given in Table 5. The slip angle estimation using the RUPF algorithm demonstrates improvements of 9.5% and 9.7% in the MAE. The *MaxAE* for the UKF and PF algorithms are approximately 0.49° , while the RUPF algorithm achieves a lower *MaxAE* of 0.439° . Regarding the *RMSE*, the estimation precision of the RUPF shows an improvement of 8.5% over the UKF and 8.7% over the PF. Compared to the high-speed DLC test performance metrics outlined in Table 3, it becomes evident that the performance metrics for the vehicle during the high-speed slalom test exhibit larger numerical values, reflecting poorer outcomes. This phenomenon can be attributed to the more extreme nature of the slalom test.

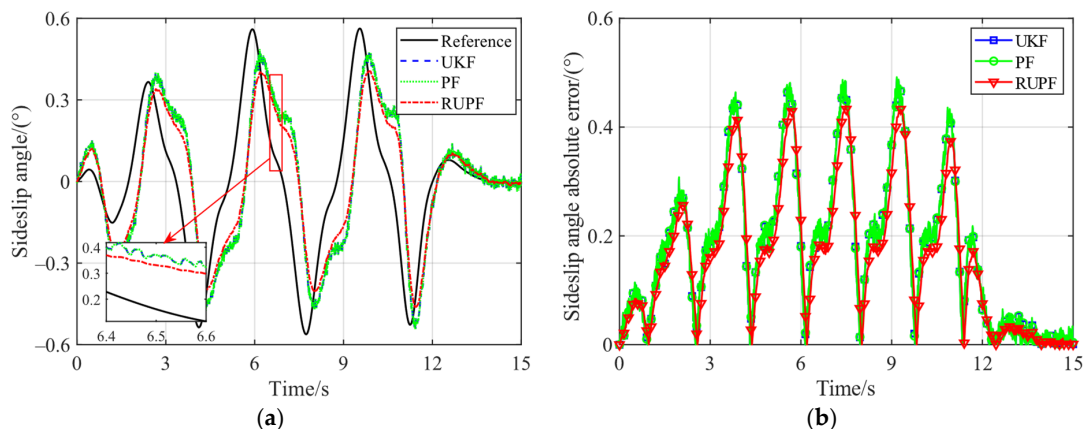


Figure 11. Simulation results of the high-vehicle-speed slalom test ($\mu = 0.85$). (a) Sideslip angle; (b) sideslip angle absolute error.

Table 5. MAE, MaxAE, and RMSE of the algorithms under the high-vehicle-speed slalom test with high road adhesion coefficient.

60 km/h	MAE	MaxAE	RMSE
UKF	0.1793	0.4894	0.2259
PF	0.1797	0.4920	0.2263
RUPF	0.1622	0.4390	0.2066

Figure 12 displays the input signals for low-vehicle-speed slalom tests.

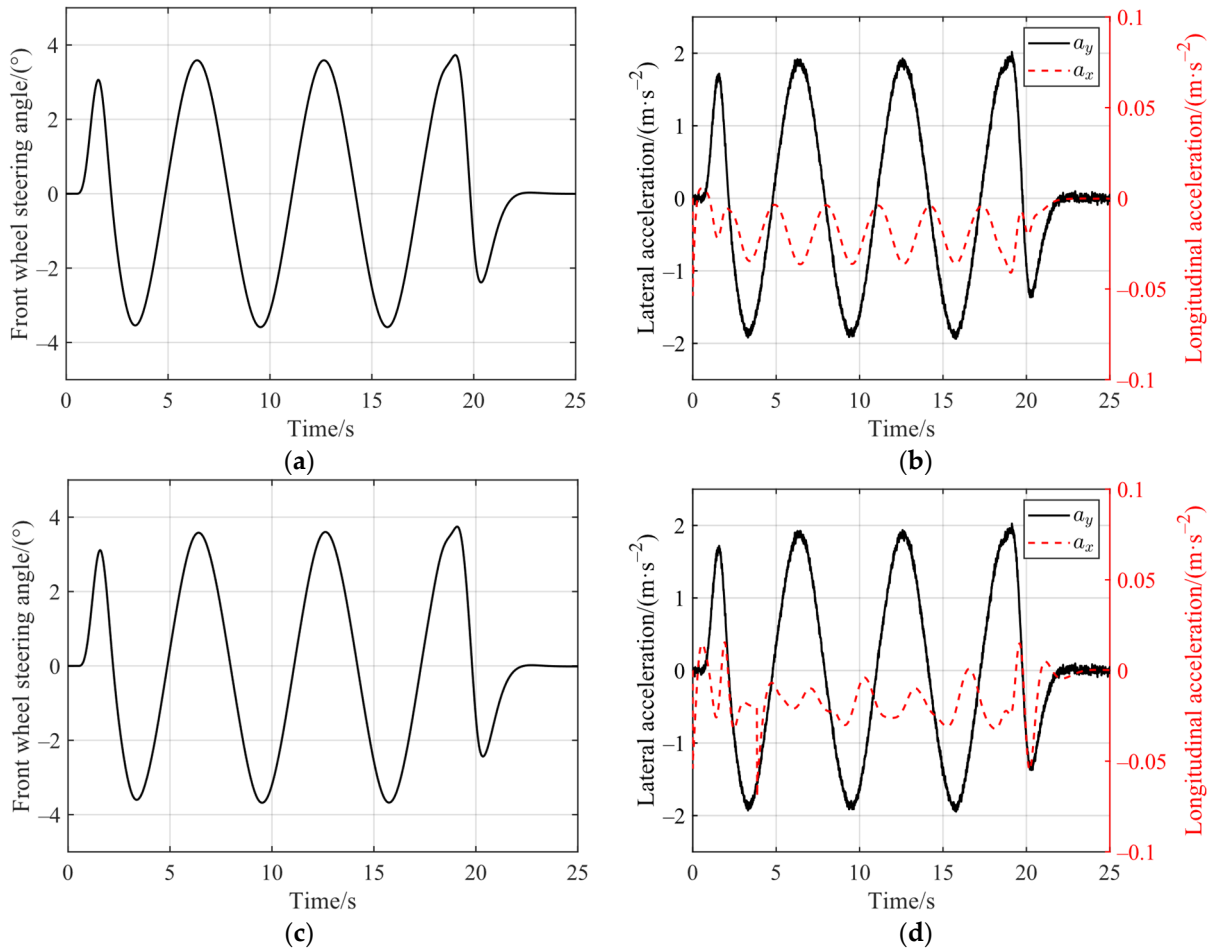


Figure 12. The inputs of low-vehicle-speed slalom tests. (a) The front wheel steering angle ($\mu = 0.85$); (b) longitudinal and lateral acceleration ($\mu = 0.85$); (c) the front wheel steering angle ($\mu = 0.35$); (d) longitudinal and lateral acceleration ($\mu = 0.35$).

The simulation outcomes for low-vehicle-speed slalom tests are presented in Figure 13. It is noteworthy that in Figure 13b, at around 20 s, the absolute errors generated by all three algorithms reach their maximum. This occurrence arises from the vehicle transitioning from the last turn to straight motion during the test. In general, the three estimation algorithms closely align with the actual values, with the estimation absolute error being less than 0.17° on high-adhesion roads and 0.18° on low-adhesion roads. Among them, the RUPF algorithm demonstrates the smallest absolute error, consistently remaining below 0.14° and 0.16° , respectively. Table 6 provides a comparison of the three metrics for the low-speed slalom tests. The estimation precision and robustness of the RUPF algorithm shows improvements of 7.4%, 19.6%, and 6.8% over the UKF and 7.2%, 20.7%, and 6.6% over the PF algorithm on the high-adhesion road surface. Meanwhile, under low-adhesion

road conditions, these metrics demonstrate respective enhancements of 5.3%, 10.0%, and 4.4% for *MAE*, *MaxAE*, and *RMSE*, and 5.2%, 10.4%, and 4.0%, respectively. Relatively speaking, the estimation performance is notably better on the high-adhesion road surface. In contrast between the assessment metrics for the low-speed DLC tests and the slalom tests, as delineated in Tables 4 and 6, the DLC tests manifest superior estimation outcomes. This disparity can be attributed to the comparatively diminished nonlinear characteristics of the vehicle during this testing scenario.

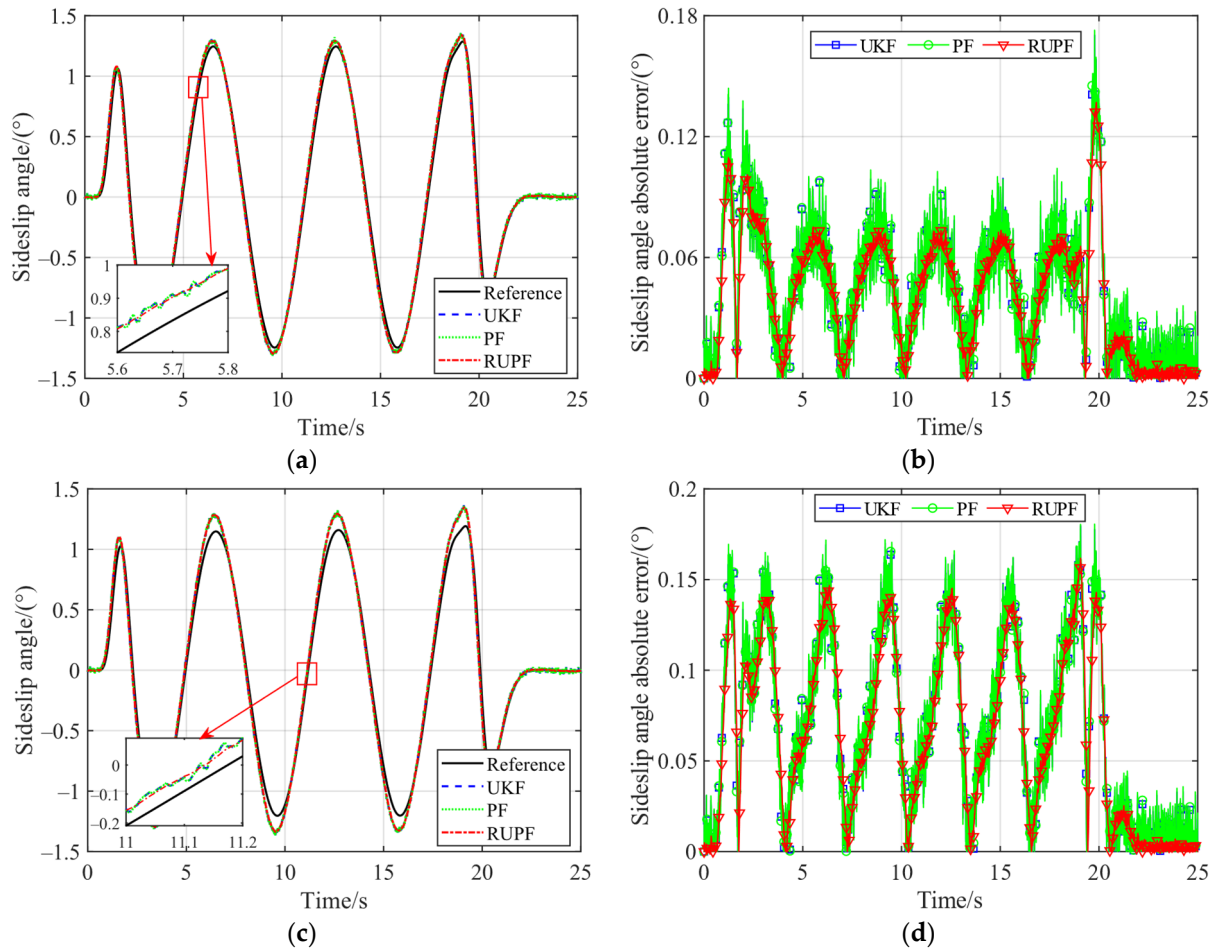


Figure 13. Simulation results of low-vehicle-speed slalom tests. (a) Sideslip angle ($\mu = 0.85$); (b) sideslip angle absolute error ($\mu = 0.85$); (c) sideslip angle ($\mu = 0.35$); (d) sideslip angle absolute error ($\mu = 0.35$).

Table 6. *MAE*, *MaxAE*, and *RMSE* of the algorithms under low-vehicle-speed slalom tests.

35 km/h	$\mu = 0.85$			$\mu = 0.35$		
	<i>MAE</i>	<i>MaxAE</i>	<i>RMSE</i>	<i>MAE</i>	<i>MaxAE</i>	<i>RMSE</i>
UKF	0.0445	0.1703	0.0544	0.0680	0.1797	0.0839
PF	0.0444	0.1728	0.0543	0.0679	0.1806	0.0835
RUPF	0.0412	0.1370	0.0507	0.0644	0.1618	0.0802

Based on the above analysis, the RUPF algorithm demonstrates notable accuracy and robustness in estimating sideslip angle under both high and low vehicle speeds and road adhesion coefficient conditions during the DLC tests and slalom tests.

5. Conclusions

This paper proposes an RUPF algorithm for estimating the vehicle sideslip angle of DDEVs based on common low-cost sensors. The RUPF algorithm accounts for uncertainties in process and measurement noises and employs the UKF to update the importance density with current, significant information in real time. Moreover, systematic random resampling is utilized to enhance the precision and robustness of the estimation. Thus, the RUPF algorithm effectively addresses the significant challenges associated with configuring the importance density and mitigating particle degradation. To validate the availability of the RUPF algorithm, simulation analyses for DLC and slalom tests were carried out in the co-simulation platform. The simulation outcomes indicate that the RUPF algorithm achieves higher precision and stronger robustness in estimating the vehicle sideslip angle under non-Gaussian noise. Compared to traditional PF and UKF algorithms, the sideslip angle estimation results of the RUPF exhibit improvements of 5.2–26.1% in *MAE*, 10.0–22.2% in *MaxAE*, and 4.0–13.6% in *RMSE* across two extreme maneuvering scenarios.

In the future, Hardware-in-the-Loop (HIL) tests or real-car experiments will be conducted to prove the real-time performance of the RUPF algorithm and its applicability within actual controllers. Furthermore, in order to realize multi-parameter joint estimation, the mutual influence mechanism between the sideslip angle and other vehicle parameters should be revealed using a sensitivity analysis.

Author Contributions: J.H.: Writing—review and editing, funding acquisition. F.R.: Methodology, writing—original draft, writing—review and editing, software. P.Z.: Supervision, funding acquisition, writing—original draft. F.Y.: supervision, resources. All authors have read and agreed to the published version of the manuscript.

Funding: This study was supported by the Key R & D project of Hubei Province (2022BAA076), Independent Innovation Projects of the Hubei Longzhong Laboratory (2022ZZ-21), and the Guangxi Science and Technology Major Program (2023AA05001).

Data Availability Statement: Data are contained within the article.

Conflicts of Interest: The authors declare no conflicts of interest.

References

1. Guo, N.; Zhang, X.; Zou, Y.; Lenzo, B.; Du, G.; Zhang, T. A supervisory control strategy of distributed drive electric vehicles for coordinating handling, lateral stability, and energy efficiency. *IEEE Trans. Transp. Electrification* **2021**, *7*, 2488–2504. [\[CrossRef\]](#)
2. Ding, X.; Wang, Z.; Zhang, L.; Wang, C. Longitudinal vehicle speed estimation for four-wheel-independently-actuated electric vehicles based on multi-sensor fusion. *IEEE Trans. Veh. Technol.* **2020**, *69*, 12797–12806. [\[CrossRef\]](#)
3. Xu, T.; Zhao, Y.; Deng, H.; Guo, S.; Lin, F. Integrated optimal control of distributed in-wheel motor drive electric vehicle in consideration of the stability and economy. *Energy* **2023**, *282*, 128990. [\[CrossRef\]](#)
4. Guo, H.; Cao, D.; Chen, H.; Lv, C.; Wang, H.; Yang, S. Vehicle dynamic state estimation: State of the art schemes and perspectives. *IEEE/CAA J. Autom. Sinica* **2018**, *5*, 418–431. [\[CrossRef\]](#)
5. Jin, X.; Yin, G.; Chen, N. Advanced estimation techniques for vehicle system dynamic state: A survey. *Sensors* **2019**, *19*, 4289. [\[CrossRef\]](#)
6. Park, G.; Choi, S.; Hyun, D.; Lee, J. Integrated observer approach using in-vehicle sensors and GPS for vehicle state estimation. *Mechatronics* **2018**, *50*, 134–147. [\[CrossRef\]](#)
7. Liu, J.; Wang, Z.; Zhang, L.; Walker, P. Sideslip angle estimation of ground vehicles: A comparative study. *IET Control Theory Appl.* **2020**, *14*, 3490–3505. [\[CrossRef\]](#)
8. Chindamo, D.; Lenzo, B.; Gadola, M. On the vehicle sideslip angle estimation: A literature review of methods, models, and innovations. *Appl. Sci.* **2018**, *8*, 355. [\[CrossRef\]](#)
9. Song, R.; Fang, Y. Vehicle state estimation for INS/GPS aided by sensors fusion and SCKF-based algorithm. *Mech. Syst. Signal Process.* **2021**, *150*, 107315. [\[CrossRef\]](#)
10. Li, L.; Jia, G.; Ran, X.; Song, J.; Wu, K. A variable structure extended Kalman filter for vehicle sideslip angle estimation on a low friction road. *Veh. Syst. Dyn.* **2014**, *52*, 280–308. [\[CrossRef\]](#)
11. Bevely, D.; Ryu, J.; Gerdes, J. Integrating INS sensors with GPS measurements for continuous estimation of vehicle sideslip, roll, and tire cornering stiffness. *IEEE Trans. Intell. Transp. Syst.* **2006**, *7*, 483–493. [\[CrossRef\]](#)

12. Chen, W.; Tan, D.; Zhao, L. Vehicle sideslip angle and road friction estimation using online gradient descent algorithm. *IEEE Trans. Veh. Technol.* **2018**, *67*, 11475–11485. [[CrossRef](#)]
13. Chindamo, D.; Gadola, M. Estimation of vehicle side-slip angle using an artificial neural network. In Proceedings of the 2nd International Conference on Mechanical, Aeronautical and Automotive Engineering (ICMAA 2018), Singapore, 24–26 February 2018. [[CrossRef](#)]
14. Gao, Z.; Wen, W.; Tang, M.; Zhang, J.; Chen, G. Estimation of vehicle motion state based on hybrid neural network. *Automot. Eng.* **2022**, *44*, 1527–1536. [[CrossRef](#)]
15. Gräber, T.; Lupberger, S.; Unterreiner, M.; Schramm, D. A hybrid approach to side-slip angle estimation with recurrent neural networks and kinematic vehicle models. *IEEE Trans. Intell. Veh.* **2019**, *4*, 39–47. [[CrossRef](#)]
16. Zha, Y.; Liu, X.; Ma, F.; Liu, C. Vehicle state estimation based on extended Kalman filter and radial basis function neural networks. *Int. J. Distrib. Sens. Netw.* **2022**, *18*, 15501329221102730. [[CrossRef](#)]
17. Boada, B.; Boada, M.; Diaz, V. Vehicle sideslip angle measurement based on sensor data fusion using an integrated ANFIS and an Unscented Kalman Filter algorithm. *Mech. Syst. Signal Process.* **2016**, *72–73*, 832–845. [[CrossRef](#)]
18. Ghosh, J.; Tonoli, A.; Amati, N. A deep learning based virtual sensor for vehicle sideslip angle estimation: Experimental results. In Proceedings of the Wcx World Congress Experience, Detroit, MI, USA, 10–12 April 2018. [[CrossRef](#)]
19. Ding, N.; Chen, W.; Zhang, Y.; Xu, G.; Gao, F. An extended Luenberger observer for estimation of vehicle sideslip angle and road friction. *Int. J. Veh. Des.* **2014**, *66*, 385–414. [[CrossRef](#)]
20. Chen, Y.; Ji, Y.; Guo, K. A reduced-order nonlinear sliding mode observer for vehicle slip angle and tyre forces. *Veh. Syst. Dyn.* **2014**, *52*, 1716–1728. [[CrossRef](#)]
21. Chen, T.; Chen, L.; Cai, Y.; Xu, X. Robust sideslip angle observer with regional stability constraint for an uncertain singular intelligent vehicle system. *IET Control Theory Appl.* **2018**, *12*, 1802–1811. [[CrossRef](#)]
22. Cheli, F.; Sabbioni, E.; Pesce, M.; Melzi, S. A methodology for vehicle sideslip angle identification: Comparison with experimental data. *Veh. Syst. Dyn.* **2007**, *45*, 549–563. [[CrossRef](#)]
23. Anderson, R.; Bevly, M. Using GPS with a model-based estimator to estimate critical vehicle states. *Veh. Syst. Dyn.* **2010**, *48*, 1413–1438. [[CrossRef](#)]
24. Reina, G.; Messina, A. Vehicle dynamics estimation via augmented extended Kalman filtering. *Measurement* **2018**, *133*, 383–395. [[CrossRef](#)]
25. Wang, P.; Pang, H.; Xu, Z.; Jin, J. On co-estimation and validation of vehicle driving states by a UKF-based approach. *Mech. Sci.* **2021**, *12*, 19–30. [[CrossRef](#)]
26. Strano, S.; Terzo, M. Constrained nonlinear filter for vehicle sideslip angle estimation with no a priori knowledge of tyre characteristics. *Control Eng. Pract.* **2018**, *71*, 10–17. [[CrossRef](#)]
27. Arasaratnam, I.; Haykin, S. Cubature Kalman Filters. *IEEE Trans. Autom. Control.* **2009**, *54*, 1254–1269. [[CrossRef](#)]
28. Xin, X.; Chen, J.; Zou, J. Vehicle state estimation using cubature Kalman filter. In Proceedings of the 2014 IEEE 17th International Conference on Computational Science and Engineering, Chengdu, China, 19–21 December 2014; pp. 44–48. [[CrossRef](#)]
29. Wang, Y.; Geng, K.; Xu, L.; Ren, Y.; Dong, H.; Yin, G. Estimation of Sideslip Angle and Tire Cornering Stiffness Using Fuzzy Adaptive Robust Cubature Kalman Filter. *IEEE Trans. Syst. Man, Cybern. Syst.* **2022**, *52*, 1451–1462. [[CrossRef](#)]
30. Chen, T.; Cai, Y.; Chen, L.; Xu, X.; Jiang, H.; Sun, X. Design of vehicle running states-fused estimation strategy using Kalman filters and tire force compensation method. *IEEE Access* **2019**, *7*, 87273–87287. [[CrossRef](#)]
31. Nishida, T.; Kogushi, W.; Takagi, N.; Kurogi, S. Dynamic state estimation using particle filter and adaptive vector quantizer. In Proceedings of the 2009 IEEE International Symposium on Computational Intelligence in Robotics and Automation (CIRA), Daejeon, Republic of Korea, 15–18 December 2009; pp. 429–434. [[CrossRef](#)]
32. Wang, B.; Cheng, Q.; Victorino, A.; Charara, A. Nonlinear observers of tire forces and sideslip angle estimation applied to road safety: Simulation and experimental validation. In Proceedings of the 2012 15th International IEEE Conference on Intelligent Transportation Systems, Anchorage, AK, USA, 16–19 September 2012; pp. 1333–1338. [[CrossRef](#)]
33. Li, T.; Sbarufatti, C.; Cadini, F. Multiple local particle filter for high-dimensional system identification. *Mech. Syst. Signal Process.* **2024**, *209*, 111060. [[CrossRef](#)]
34. Kuptamete, C.; Michalopoulou, Z.; Aunsri, N. A review of efficient applications of genetic algorithms to improve particle filtering optimization problems. *Measurement* **2024**, *224*, 113952. [[CrossRef](#)]
35. Huang, F.; Gao, Y.; Fu, C.; Gostar, A.K.; Hu, M. Vehicle state estimation based on adaptive state transition model. In Proceedings of the 2020 4th CAA International Conference on Vehicular Control and Intelligence (CVCI), Hangzhou, China, 18–20 December 2020; pp. 92–96. [[CrossRef](#)]
36. Zhang, Y.; Li, M.; Zhang, Y.; Hu, Z.; Sun, Q.; Lu, B. An enhanced adaptive unscented Kalman filter for vehicle state estimation. *IEEE Trans. Instrum. Meas.* **2022**, *71*, 6502412. [[CrossRef](#)]
37. Fu, Z.; Luo, Z. A vehicle driving state estimation algorithm based on Elman neural network and unscented Kalman filter. In Proceedings of the 2021 IEEE 5th Advanced Information Technology, Electronic and Automation Control Conference (IAEAC), Chongqing, China, 12–14 March 2021; pp. 415–419. [[CrossRef](#)]
38. Chen, T.; Chen, L.; Xu, X.; Cai, Y.; Jiang, H.; Sun, X. Estimation of longitudinal force and sideslip angle for intelligent four-wheel independent drive electric vehicles by observer iteration and information fusion. *Sensors* **2018**, *18*, 1268. [[CrossRef](#)] [[PubMed](#)]

39. *ISO 3888-2:2018*; Passenger Cars–Test Track For A Severe Lane–Change Manoeuvre–Part 1: Double Lane–Change. International Organization for Standardization (ISO): Geneva, Switzerland, 2018.
40. *ISO 15037-1:2019*; Road Vehicles–Vehicle Dynamics Test Methods–Part 1: General Conditions for Passenger Cars. International Organization for Standardization (ISO): Geneva, Switzerland, 2019.

Disclaimer/Publisher’s Note: The statements, opinions and data contained in all publications are solely those of the individual author(s) and contributor(s) and not of MDPI and/or the editor(s). MDPI and/or the editor(s) disclaim responsibility for any injury to people or property resulting from any ideas, methods, instructions or products referred to in the content.